Modeling of plasma dynamics at the air-water interface: Application to laser shock processing

V. I. Mazhukin and V. V. Nossov
Institute of Mathematical Modeling of RAS, 4a Miusskaya sqr., 125047 Moscow, Russia

I. Smurov[a)]
Ecole Nationale d'Ingénieurs de Saint-Etienne, 58 rue Jean Parot, 42023 Saint-Etienne Cedex 2, France

(Received 19 October 2000; accepted for publication 12 April 2001)

The gas-dynamic expansion stage of the plasma at the air-water interface is studied numerically for the setup corresponding to the laser shock processing of materials in the water-confined regime. The plasma is induced by a laser radiation of the intensity range 4–17 GW/cm^2 at the 1.06 and 0.353 μm laser wavelength. A mathematical description of the plasma is performed in the frame of transient two-dimensional radiative gas dynamics, which incorporates the system of gas-dynamic equations and the radiation transfer equation. The studies performed indicate that the plasma evolution significantly depends on the laser wavelength. For the IR laser effect the expansion mechanism is the fast propagation of the ionization wave toward the laser source, and for the UV laser effect the laser supported detonation wave is formed. The plasma radiation contributes significantly to the redistribution of energy inside the plasma domain and, for the UV effect, forms the domain of preionization ahead of the shock wave. In both cases the plasma becomes opaque: for the IR effect it occurs over a very short period of time, 3–5 ns, while for the UV effect the process takes much longer. When the laser intensity is increased, the peak intensity and the duration of the transmitted pulse tend to reach a saturation level. © *2001 American Institute of Physics.*
[DOI: 10.1063/1.1378061]

I. INTRODUCTION

A number of promising applications for the laser shock processing (LSP) of materials placed in weakly absorbing media (e.g., water or alcohol solutes)[1–3] initiated intensive studies of laser radiation interaction with solid targets and water.[4–8] The investigations performed revealed the great variety and complexity of the phenomena involved. Qualitative and quantitative regularities of the process change depending on the main laser parameters: wavelength, peak intensity, pulse duration, time, and space intensity distribution.

Laser-water interaction proceeds in thermal mode for as long as the intensity G is less than 10^6 W/cm^2. Once the intensity has exceeded 10^6 W/cm^2 the heating is accompanied by evaporation. Both regimes are characterized by the formation and propagation of photoacoustic signals. In particular, complex high-frequency oscillations imposed on basic acoustic signal were observed at irradiation of water by long pulses ($\tau \approx 3$ μs) of CO_2 laser, for the thermal ($G \approx 3 \times 10^5$ W/cm^2) and evaporation ($G \approx 2.5 \times 10^6$ W/cm^2) modes.[9] It was shown that the oscillations result from weak intensity modulation on the trailing edge of the laser pulse. The transition to shorter (0.2–0.3 μs) and higher intensity ($\sim 10^7$ W/cm^2) pulses led to the disappearance of the oscillations and the generation of a bipolar acoustic signal of great amplitude ~30–60 bar. When laser pulses with a steep trailing edge were applied, a strong negative pressure signal was generated with the amplitude several times that of the original positive signal. If the negative pressure exceeds a certain threshold value it causes instability of deflagration or the Rayleigh–Taylor type.[10,11]

The transition to nanosecond range of pulse duration and intensities of $G > 10^9$ W/cm^2 is characterized by plasma formation near the target surface with typical pressure $p \approx (1-5) \times 10^4$ bar and generation of high-power shock wave.[4–6] The pressure pulse of the plasma can be utilized, for example, to improve the fatigue behavior of aluminum alloys and to post-treat the CO_2 laser-quenched steel surface.[2]

One of the main problems of LSP is to increase the power and duration of the pressure pulse. The application of the transparent liquid layer placed onto the treated surface presents an effective technique to reach this objective [Fig. 1(a)]. From one side, the liquid slows down evaporation and prevents removal of the absorbed energy by the flow of evaporated substance. The instantaneously heated layer has no time to expand and all the energy converts into compressive stress. Also, the dense liquid medium confines the expansion of the plasma formed near the interface, which leads to the further increase of the amplitude and duration of the pressure pulse.[5] Another direction of the LSP efficiency increase is the application of nanosecond laser pulses with an intensity of 10^{10}–10^{12} W/cm^2.[7]

A limiting factor of the confining layer application is the formation of secondary plasma at the air-water interface [Fig. 1(a)]. The plasma partially or completely absorbs the incident laser pulse and as a result the pulse that actually affects the target (transmitted) becomes shorter and weaker than the incident one. A detailed analysis of the transmission

a)Electronic mail: smurov@enise.fr

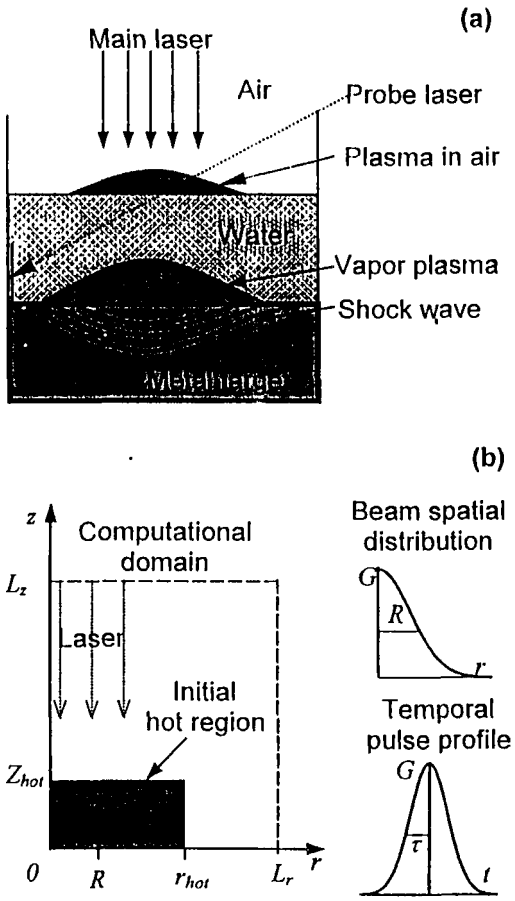

FIG. 1. (a) Scheme of laser shock processing in the water-confined regime accompanied by the breakdown plasma initiation in air and probing of the plasma transmission; (b) coordinate frame, configuration of computational domain and laser beam parameters. Laser pulses have Gaussian distributions of intensity on space and time with $\tau = 1.7 \times 10^{-8}$ s and $R = 0.15$ cm and peak intensities of $G_0' = 4-17$ GW/cm^2.

of the air plasma induced by the laser pulse with duration of 25–30 ns at a wavelength of 1.06 μm was performed in Ref. 8. The technique was proposed to estimate the parameters of the transmitted pulse by means of the transmission measurements of the probe radiation [Fig. 1(a)].

Plasma formation near the surface of a target irradiated by micro- and nanosecond laser pulses was studied in a number of experimental and theoretical papers.[12–16] It was shown that the evolution of the plasma is strongly coupled with the target ablation and proceeds in significantly different ways as compared to plasma in pure gaseous medium. The performed experiments revealed the complex structure of plasma patterns and essential differences between the expansion of plasma initiated by IR ($\lambda = 1.06$ μm) and UV ($\lambda = 0.308$ μm) lasers.[15,16]

The theoretical description of the plasma is complicated if the plasma radiation significantly contributes to the energy balance. Under this condition, variable opacity plasma should be described by models of radiative gas dynamics (RGD), which incorporates the system of gas dynamic equations and the radiation transfer equation (RTE).[17–20]

The expansion of laser plasma can proceed in various conditions (regimes) depending on laser pulse and gas parameters.[18] For laser supported combustion regimes the plasma is characterized by the temperature of a few electron volts, the subsonic velocity of expansion and low pressure close to the pressure of undisturbed gas. The main mechanisms of energy transfer are heat conductivity and subsonic radiation wave. On the other hand, for detonation regimes [laser supported detonation (LSD) wave, supersonic radiation wave, ionization wave, and their different combinations] the high temperature ($T \sim 10$ eV), high pressure differences (hundreds and thousands of bars) and supersonic velocities of plasma pattern propagation are realized.

The analysis of laser plasma evolution by means of RGD models was performed in Refs. 21–27. The two-dimensional (2D) expansion of air plasma into the environment at a pressure of 1–100 bar was studied in Refs. 21 and 22. It was established that the expansion mechanism changes based on a value of counter-pressure: from the LSD regime at low pressure to subsonic radiation wave at high pressure. The same model was applied to compare the expansion of plasma in aluminum vapor and air.[23]

Neither of the regimes described earlier is separately realized for plasma formed near the ablated surface. A correct description of the plasma in this case requires the application of a two-component model, which describes processes in both condensed and gaseous media. The model was used in Refs. 24 and 25 to study how plasma affects evaporation. The plasma screening, thermal and gas-dynamic effects were determined. In particular, it was shown that the plasma pressure can completely suppress the evaporation from the target surface at a temperature much higher than the equilibrium boiling temperature. The two-dimensional RGD model of plasma combined with the one-dimensional model of target heating, melting and evaporation was presented in Refs. 26 and 27. A detailed description of the plasma radiation effect on the process described was given.

Thus, laser plasma is characterized by a variety of processes, the relative contribution of which is not known in advance and should be determined. Mathematical modeling provides an effective tool for the analysis of such problems. The main purpose of this study is to model a plasma at the air-water interface under typical LSP conditions and to determine the regularities of plasma expansion, absorption, and transmission. The effect of Nd–yttrium–aluminum–garnet laser is considered at wavelengths of 1.06 and of 0.353 μm, pulse duration of 34 ns, and intensity range of 4–17 GW/cm^2.

The article is organized as follows: The second part contains the problem statement based on the 2D RGD model in the cylindrical coordinate frame. The model consists of: (i) a system of equations governing inviscid nonheat-conducting gas flow; (ii) a radiation transfer equation considered in diffusion multigroup approximation; (iii) Saha–Eggert equations for the determination of plasma charge composition; and (iv) the equations of the state and optical properties of the plasma. The third part contains an analysis and discussion of the results. The typical distribution of temperature, density, and electron concentration are shown, the mechanisms of plasma expansion for IR and UV range effect are established, the parameters of transmitted laser pulses and

their variation with laser fluency are determined. As a conclusion, the main results of the study are briefly formulated.

II. MATHEMATICAL MODEL

A. Problem setup and principal assumptions

The physical setup considered is similar to the one in the experiment described by Ref. 8 [Fig. 1(a)]. A metal target is covered by a layer of water. Laser light incidents on the target and causes the formation of two plasmas near the target surface and air-water interface. A self-consistent model of the system should simultaneously describe processes in the metal target, water, and air. However, the numerical implementation of such a model in the 2D case faces great computational difficulties. Considering that the processes in the air plasma present the main subject of the research, the problem can be essentially simplified by assuming that a thin plasma layer already exists above the water surface at the beginning of the study. This assumption allows us to exclude the water layer and to analyze just the air plasma by means of the 2D RGD model.[19,22]

The problem has axial symmetry and is solved in the cylindrical coordinate frame introduced in the air domain [Fig. 1(b)]. The plasma modeling is based on the following assumptions:

(1) A thin plasma layer at temperature $T=T_{\text{hot}}$ and density $\rho=\rho_{\text{hot}}$ exists near the air-water interface at initial point of time;
(2) Plasma is considered to be the absorbing medium and local thermodynamic equilibrium conditions are fulfilled; and
(3) The expansion of plasma is described in an inviscid, nonheat-conducting gas approximation.

B. Gas-dynamic expansion

The movement of the plasma is described by the conservation equations for mass, momentum, and energy

$$\frac{\partial \rho}{\partial t}+\frac{1}{r}\frac{\partial}{\partial r}(r\rho u)+\frac{\partial}{\partial z}(\rho v)=0, \tag{1}$$

$$\frac{\partial(\rho u)}{\partial t}+\frac{1}{r}\frac{\partial}{\partial r}(r\rho u^2)+\frac{\partial}{\partial z}(\rho u v)=-\frac{\partial(p+\omega)}{\partial r}, \tag{2}$$

$$\frac{\partial(\rho v)}{\partial t}+\frac{1}{r}\frac{\partial}{\partial r}(r\rho u v)+\frac{\partial}{\partial z}(\rho v^2)=-\frac{\partial(p+\omega)}{\partial z}, \tag{3}$$

$$\frac{\partial(\rho \epsilon)}{\partial t}+\frac{1}{r}\frac{\partial}{\partial r}(r\rho u \epsilon)+\frac{\partial}{\partial z}(\rho v \epsilon) =-p\left[\frac{1}{r}\frac{\partial(ru)}{\partial r}+\frac{\partial v}{\partial z}\right]-\left[\frac{1}{r}\frac{\partial W_r}{\partial r}+\frac{\partial W_z}{\partial z}\right]+\left[\frac{\partial G}{\partial z}\right], \tag{4}$$

$$p=p(\rho,T), \quad \epsilon=\epsilon(\rho,T). \tag{5}$$

Here t, r, and z are the time and space coordinates; ρ stands for the density; u, v are the components of the velocity vector; p, ω denote the pressure and artificial viscosity; ϵ represents the specific internal energy; W_r, W_z are the components of the total radiative heat flux; and G denotes the laser intensity. Three terms in brackets in the right-hand side of Eq. (4) describe three components of the plasma energy balance: work of pressure force, radiation cooling, and laser light absorption.

The equation system is subjected to the following initial and boundary conditions:

$$t=0: \quad u=v=0, \quad 0\leqslant(r,z)\leqslant(L_r,L_z),$$
$$T=T_{\text{hot}}, \quad \rho=\rho_{\text{hot}}, \quad 0\leqslant(r,z)\leqslant(l_r,l_z), \tag{6}$$
$$T=T_0, \quad \rho=\rho_0, \quad (l_r,l_z)<(r,z)\leqslant(L_r,L_z)$$

$$r=0: \quad u=0, \quad \partial\rho/\partial r=\partial v/\partial r=\partial P/\partial r=0; \tag{7}$$

$$z=0: \quad v=0, \quad \partial\rho/\partial z=\partial u/\partial z=\partial P/\partial z=0; \tag{8}$$

$$r=L_r: \quad p=p_0, \quad \rho=\rho_0, \quad u=v=0; \tag{9}$$

$$z=L_z: \quad p=p_0, \quad \rho=\rho_0, \quad u=v=0. \tag{10}$$

C. Plasma radiation transfer

The steady-state RTE is written as follows:

$$\mathbf{\Omega}\,\text{grad}\,I_\nu+\kappa_\nu I_\nu=\kappa_\nu I_{\nu,\text{eq}}, \tag{11}$$

where $\mathbf{\Omega}$ is the unit direction vector; I_ν, $I_{\nu,\text{eq}}$ are the spectral radiative intensity and spectral blackbody intensity (Planck function); and κ_ν denotes the absorption coefficient. The main complexity of the Eq. (11) is due to its higher dimensionality, as compared to other parts of the model, because the unknown function I_ν additionally depends on $\mathbf{\Omega}$ and ν variables. However, the problem can be substantially simplified if the low anisotropy of plasma optical properties is assumed and diffusion approximation is applied to the description of radiation transfer[20]

$$\text{div}\,\mathbf{W}_\nu+c\kappa_\nu U_\nu=c\kappa_\nu U_{\nu,\text{eq}},$$
$$c/3\,\text{grad}\,U_\nu+\kappa_\nu \mathbf{W}_\nu=0, \tag{12}$$

where c is the speed of light; $\mathbf{W}_\nu$ is the spectral radiative heat flux, and U_ν, $U_{\nu,\text{eq}}$ are spectral energy density of radiation and blackbody radiation

$$U_{\nu,\text{eq}}=\frac{8\pi h\nu^3}{c^3(\exp(h\nu/kT)-1)}. \tag{13}$$

The second step of transformation of the Eqs. (11) and (12), that depend on radiation frequency ν, is the application of multigroup approximation.[21,28] In the approach, the frequency range is divided to a finite number of intervals (groups), the unknown functions $\mathbf{W}_\nu$, U_ν are assumed to be independent of frequency within the intervals, and κ_ν, $U_{\nu,\text{eq}}$ are substituted by frequency averaged values

$$[\nu_{\min},\nu_{\max}]=\sum_{k=1}^{N}[\nu_{k-1},\nu_k],$$

$$\nu\in[\nu_{k-1},\nu_k]: \quad \mathbf{W}_\nu\equiv\mathbf{W}_k, \quad U_\nu\equiv U_k,$$

$$U_{k,\text{eq}}=\int_{\nu_{k-1}}^{\nu_k} U_{\nu,\text{eq}}\,d\nu.$$

Finally, the initial RTE is transformed into the system of N equations that depend only on time and space coordinates

$$\operatorname{div}\mathbf{W}_k + c\kappa_k U_k = c\kappa_k U_{k,\mathrm{eq}}, \quad k = 1,N,$$

$$\mathbf{W}_k = -\frac{c}{3\kappa_k}\operatorname{grad} U_k, \quad \mathbf{W} = (W_r, W_z) = \sum_{k=1}^{N} \mathbf{W}_k, \quad (14)$$

$$U = \sum_{k=1}^{N} U_k.$$

Boundary conditions for the radiation transfer model are set as

$$\begin{aligned} &r=0: \quad W_r = 0, \\ &z=0: \quad W_z = +cU/2, \\ &r=L_r: \quad W_r = cU/2, \\ &r=L_z: \quad W_z = cU/2. \end{aligned} \quad (15)$$

The absorption coefficient of the plasma $\kappa_\nu = \kappa_\nu(h\nu, T, \rho,)$ depends on the radiation frequency, temperature, and density of plasma, and is contributed to by several absorption mechanisms. In our studies κ_ν is calculated in advance on the quantum-mechanical Hartree–Fock–Slater model[29] for the following range of parameters: $T \in (0.01-250\,\mathrm{eV})$, $\rho \in (5\times10^{-6}-10^{-2}\,\mathrm{cm}^{-3})$, $h\nu \in (0.01-250\,\mathrm{eV})$. The results are presented in the form of three-dimensional tables. The number of spectral groups N is equal to 10. Within each group $\nu \in [\nu_{k-1}\nu_k]$ the Planck or Rosseland mean absorption coefficients are used, determined as

$$\kappa_k = \frac{\int_{\nu_{k-1}}^{\nu_k} \kappa_\nu U_{\nu,\mathrm{eq}} d\nu}{\int_{\nu_{k-1}}^{\nu_k} U_{\nu,\mathrm{eq}} d\nu}; \quad \kappa_k^{-1} = \frac{\int_{\nu_{k-1}}^{\nu_k} \kappa_\nu^{-1} (\partial U_{\nu,\mathrm{eq}}/\partial T) d\nu}{\int_{\nu_{k-1}}^{\nu_k} (\partial U_{\nu,\mathrm{eq}}/\partial T) d\nu}.$$

The equations of the state (5) are determined using the same model and were presented in form of two-dimensional tables.[30]

D. Laser radiation transfer

The absorption of the laser radiation as the beam propagates parallel to the z axis is described by the transfer equation

$$\frac{\partial G}{\partial z} - \kappa G = 0, \quad (16)$$

with boundary condition

$$z = L_z: \quad G = G_0 \exp[-(t/\tau)^2]\exp[-(r/R)^2], \quad (17)$$

where τ denotes the half width at half maximum of the pulse and R is the laser beam radius. The absorption coefficient of laser radiation κ in the IR range is specified by the following formula:[20,31]

$$\kappa = \frac{8\pi e^6}{3mhc(6\pi mk)^{1/2}} \frac{N_e \sum_{l=1}^{L_{\max}} l^2 N_l}{\nu^3 T^{1/2}} \left[1 - \exp\left(-\frac{h\nu}{T}\right)\right], \quad (18)$$

where N_e and N_z are the concentration of electrons and ions with charge l (the $l=0$ index corresponds to neutrals); $L_{\max}$ denotes the maximum charge of ions accounted in the model; h, m, and e are the Planck's constant, mass and charge of an electron, accordingly. Formula (18) describes the absorption of laser radiation by electron gas through the inverse Bremsstrahlung mechanism, and accounts for the absorption of photons due to electron-ion interactions. The mechanism by electron-neutral interactions that is important mostly in weakly ionized gases is neglected. For the UV range the tabular values of respective spectral groups are used.

The charge composition of the plasma is determined from the Saha–Eggert equations[20,31]

$$\frac{N_e N_l}{N_{l-1}} = \frac{g_e g_l}{g_{l-1}} \left(\frac{mT}{2\pi\hbar^2}\right)^{3/2} \exp(-J_l/T), \quad l = 1,\ldots,L_{\max} \quad (19)$$

with g_e, g_l being the statistical weights of electrons and ions and J_l denotes ionization potential.

The numerical solution of the problem is performed by the finite-difference method that is presented in detail in Ref. 22. The algorithm consists of the main cycle on the time variable, and each time step includes three stages: (i) the solution of the radiation diffusion equations for each frequency group; (ii) the coupled solution of the averaged equation of the radiation diffusion and the energy equation; and (iii) the solution of gas-dynamic equations.

III. RESULTS AND DISCUSSION

A. Onset of the process and initial conditions

The domain $0 \leqslant (r,z) \leqslant (L_r, L_z)$ is considered to be filled by still air at temperature $T(0,r,z) = T_0$ and density $\rho(0,r,z) = \rho_0$, [Fig. 1(b)]. The plane $z=0$ corresponds to the water surface. Laser pulses are single, have wavelengths $\lambda = 1.06$ μm or $\lambda = 0.353$ μm, Gaussian distribution of intensity on space and time, [Fig. 1(b)], $\tau = 1.7\times10^{-8}$ s, $R = 0.15$ cm, and peak intensities G_0 of 4–17 GW/cm^2.

According to the assumption accepted, the initial hot domain $0 \leqslant (r,z) \leqslant (r_{\mathrm{hot}}, z_{\mathrm{hot}})$ is specified along the water surface $T(0,r,z) = T_{\mathrm{hot}}$ and $\rho(0,r,z) = \rho_{\mathrm{hot}}$, that corresponds to water evaporation, the optical breakdown of evaporated matter, and plasma initiation. Here $r_{\mathrm{hot}} < L_r$, $z_{\mathrm{hot}} \ll L_z$, $T \gg T_0$, $\rho_{\mathrm{hot}} = \rho_0$. The following values of the earlier parameters are used in computations: $L_r = 5$ cm, $L_z = 10$ cm, $r_{\mathrm{hot}} = 2R$, $T_0 = 0.03$ eV, $\rho_0 = 1.25\times10^{-3}$ g/cm^{-3}.

The setting of T_{hot} and l_z values for the IR effect is performed by means of adjusting computational and experimental dependencies of transmission of the probing laser radiation. At fixed intensity G_0 the (T_{hot}, l_z) pair is chosen to ensure that the numerically determined transmission coefficient becomes equal to 0.5 at the same time (referred to as the cutoff time) as in the experiment.[8,32,33] Appropriate data are compiled in Table I. As one may conclude from the data presented, the temperature of the initial hot domain is the principal factor in respect to transmission predictions. The value of this quantity changes near the 1 eV. The influence of the domain thickness l_z is much weaker and its increase from 50 to 100 μm requires a reduction of the temperature T_{hot} by 5%. At the T_{hot} below 0.9 eV plasma is not formed at any intensity from the considered range.

For the UV effect the initial data are specified less accurately, because direct observations of plasma transmission for

TABLE I. Setting the parameters of the initial hot domain, $\lambda = 1.06\ \mu$m. The following data are presented for each value of the peak power density G_0: the experimental value of the cutoff time t_0, the thickness l_z, and temperature T_{hot} of the initial hot domain used in the computations.

		Initial hot domain parameters	
Peak power density G_0 (GW/cm^2)	Cutoff time t_0 (ns)	$l_z = 50\ \mu$m T_{hot} (eV)	$l_z = 100\ \mu$m T_{hot} (eV)
6	10–15	1.05	0.98
10	0	1.05	0.98
13	13	1.1	1.02

this regime are not available. However, based on pressure pulse measurements,.one can estimate that radiation screening at the peak of the laser pulse $t_{tr} \approx 0$ ns takes place at the intensity $G_0 = 6$ GW/cm^2.[7,32] The situation is reproduced numerically if the initial hot domain is specified with parameters $T_{hot} = 2$ eV and $l_z = 100\ \mu$m.

A nonuniform grid is applied in the computations with 40–60 nodes on the r coordinate and 50–100 on the z coordinate. The typical running time on PC PIII-500 ranges from tens of minutes to several hours.

B. Mechanisms of plasma pattern expansion

The regularities of plasma expansion are analyzed using computations performed for a laser pulse of $G_0 = 10$ GW/cm^2 at two wavelengths $\lambda = 1.06\ \mu$m (referred to as IR effect) and $\lambda = 0.353\ \mu$m (UV effect), Figs. 2–12.

The distributions of temperature, density and electron concentration at $t = 0$ ns for the IR effect are shown in Fig. 2. The intensive absorption of laser radiation causes fast temperature rise in the initial hot domain $T_{max} \approx 10$ eV [Fig. 2(a)]. Overpressure in the domain leads to the formation of a shock wave along the boundary with the undisturbed air [Fig. 2(b)]. The maximum density at the shock wave front reaches 3×10^{-3} g/cm^3, and exceeds the background density more than twice. The electron concentration also increases and has a maximum of $\approx 10^{20}$ cm^{-3} at the shock wave [Fig. 2(c)]. The later stage of the process $t = 34$ ns $= 2\tau$ is presented in Fig. 3. For the IR effect, the energy-input rate appears to be sufficient to cause the formation of an ionization wave:[18] the region of high temperature and electron concentration [Figs. 3(a) and 3(c)] that propagates at high speed while the density of the gas remains unchanged [Fig. 3(b)].

Plots of the shock wave and ionization fronts for the IR effect are shown in Fig. 4. Locations of the fronts are determined on the axis of the laser beam ($r = 0$): the ionization front coordinate is calculated from the condition $\alpha = N_e/N_0 = 0.01$ (where N_e and N_0 are the electrons and neutral concentrations), and the shock wave coordinate corresponds to the maximum pressure. The ionization wave is the fastest regime of plasma expansion: as seen in Fig. 4 it propagates at a high speed ≈ 100 km/s, which is a much higher than the speed of sound. The shock wave is governed by slower gasdynamic processes and, as a result, moves at a much lower speed. After termination of the laser pulse the ionization

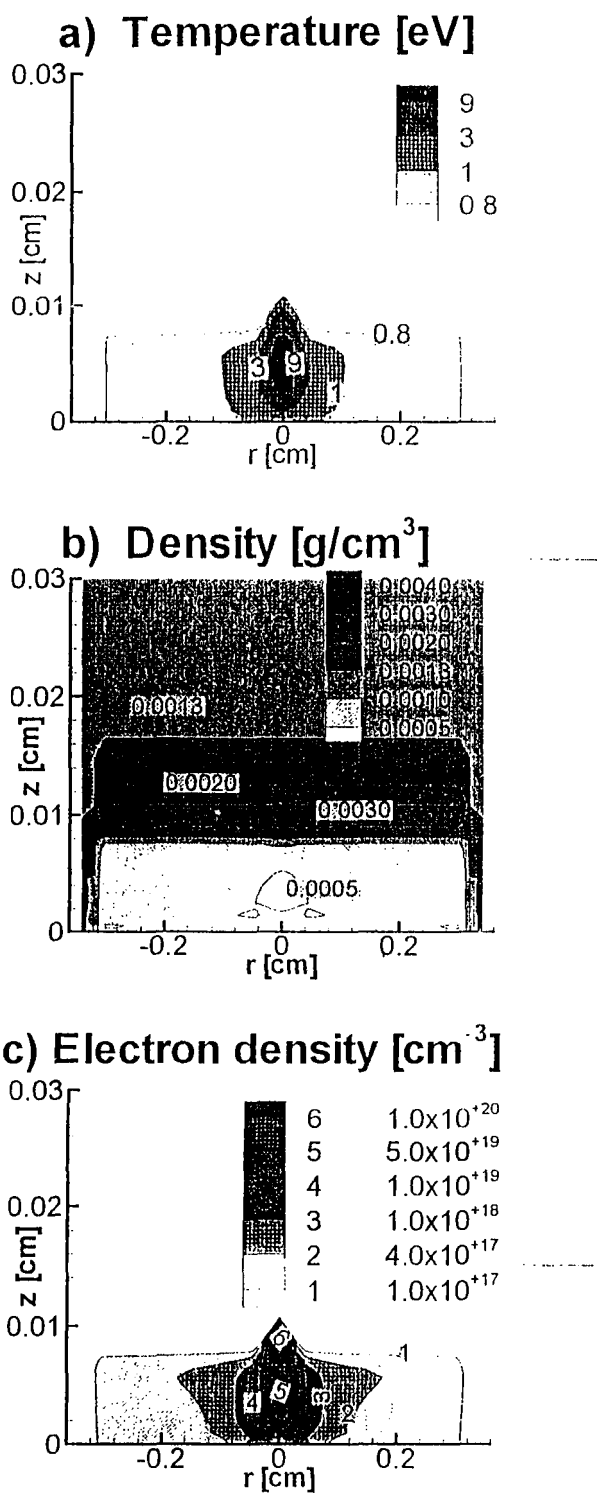

FIG. 2. Contour plots in the computational domain subjected to laser pulse at $\lambda = 1.06\ \mu$m, at $t = 0$ ns (peak of the pulse): (a) temperature, (b) density, and (c) electron concentration.

front decelerates abruptly, the shock wave overtakes it, and starting from the instant $t \approx 200$ ns the plasma expansion is characterized by one front.

The energy balance of the plasma consists of three components: the laser radiation energy, the energy of plasma radiation, and the work of pressure. The specific mechanism of plasma expansion is in fact determined by the relative con-

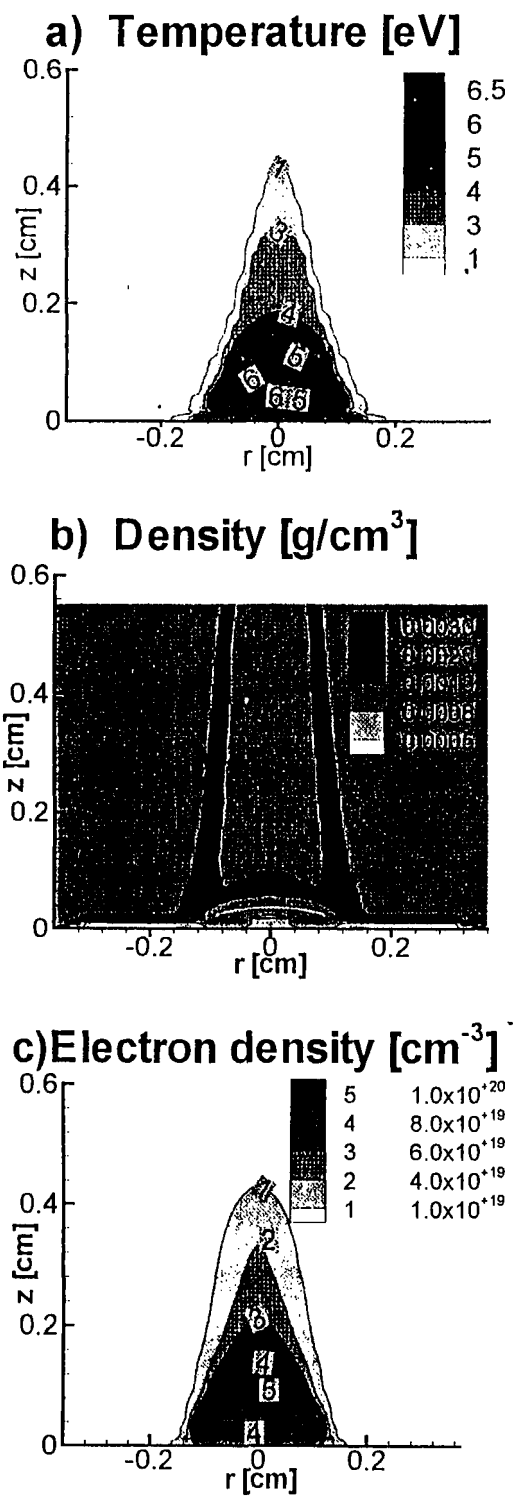

FIG. 3. Contour plots in the computational domain subjected to laser pulse at $\lambda=1.06$ μm, $t=34$ ns (completion of the pulse): (a) temperature, (b) density, and (c) electron concentration.

tributions of these components. For the IR effect, the laser radiation energy dominates at the vicinity of the ionization front, and the work of the pressure is the main factor in the shock wave domain. The contribution of the plasma radiation is illustrated by the two $T(z)$ dependencies (Fig. 5), taken at the $r=0$, $t=17$ ns. The dependence presented by the solid line is determined by the full model (1)–(19), and the dashed

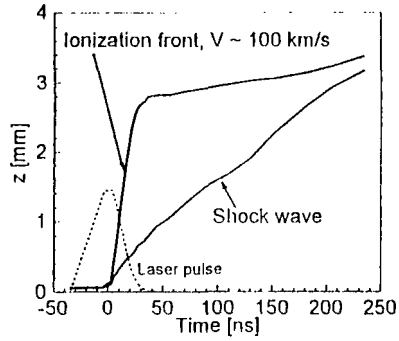

FIG. 4. Coordinates of the shock wave and ionization front, $\lambda=1.06$ μm.

line corresponds to the model that does not account for the plasma radiation transfer. As follows from these results, the plasma radiation effectively redistributes energy in the hot domain between the water surface and the shock wave. With the radiation transfer excluded, the shock wave front becomes sharper, and the temperature raises by $\approx$2 eV. In the domain of the ionization front, on the other hand, the contribution of radiation is negligible. The temperature of the domain is 2–3 eV and the spectral maximum of emitted radiation falls to the 6–8 eV range. The cold air absorbs very weakly in this range and the radiation leaves the plasma pattern unaffected.

Presented in Fig. 6 are several plots of the shock wave movement: predicted numerically (solid line), determined experimentally by high speed photography[32] (dotted line), and calculated from the analytic solution for plasma propagation speed D[18] (dashed line)

$$D=[2(\gamma^2-1)G_0/\rho]^{1/3},$$

where $\gamma=c_p/c_v\approx 1.4$ for the hot air. The numerical and experimental values coincide well. The analytic dependence, derived for constant intensity irradiation, correctly describes the front movement at the early stage of the process and becomes less accurate at the later stage.

Gas-dynamic characteristics of the process: distribution of pressure $P(z,r=0)$, normal $V_z(z,r=0)$, and radial $V_r(r,z=55\,\mu\text{m})$ velocity components are shown in Fig. 7. The initial period of the plasma formation is characterized by fast pressure rise that reaches several kilobars [Fig. 7(a), curve 1]. Further on, the high-pressure domain propagates

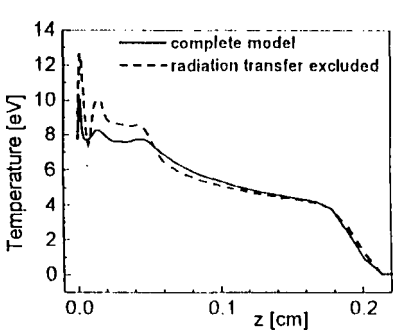

FIG. 5. Temperature distribution $T(z,r=0)$ at $t=17$ ns determined by the complete model (solid line), and by the model with radiation transfer excluded (dashed line), $\lambda=1.06$ μm.

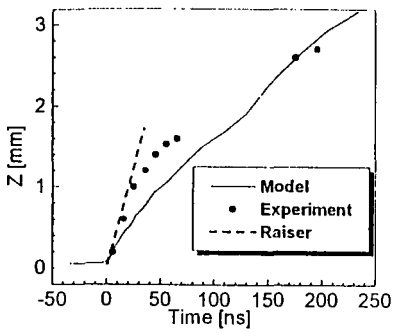

FIG. 6. Coordinates of the shock wave, $\lambda = 1.06$ μm: predicted numerically (solid line), determined experimentally (see Ref. 32) (dotted line), analytic solution (see Ref. 18) (dashed line).

with the ionization wave and reaches its maximum at the shock wave front [Fig. 7(a), curve 2]. As the plasma cools down, the pressure also decreases very rapidly [Fig. 7(a), curve 3, 4]. The curves of the normal velocity are bipolar [Fig. 7(b)]: the positive branch corresponds to the shock wave and the negative one to the compression wave, which moves toward the water surface. The shock wave speed is

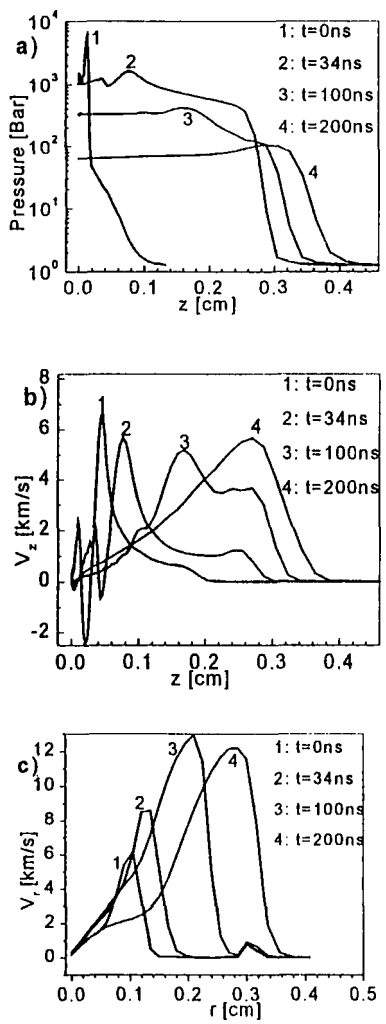

FIG. 7. Distributions of pressure $P(z, r=0)$ (a), velocity components $V_z(z, r=0)$ (b), and $V_r(r, z=55$ μm) (c) at several instants of time, $\lambda = 1.06$ μm.

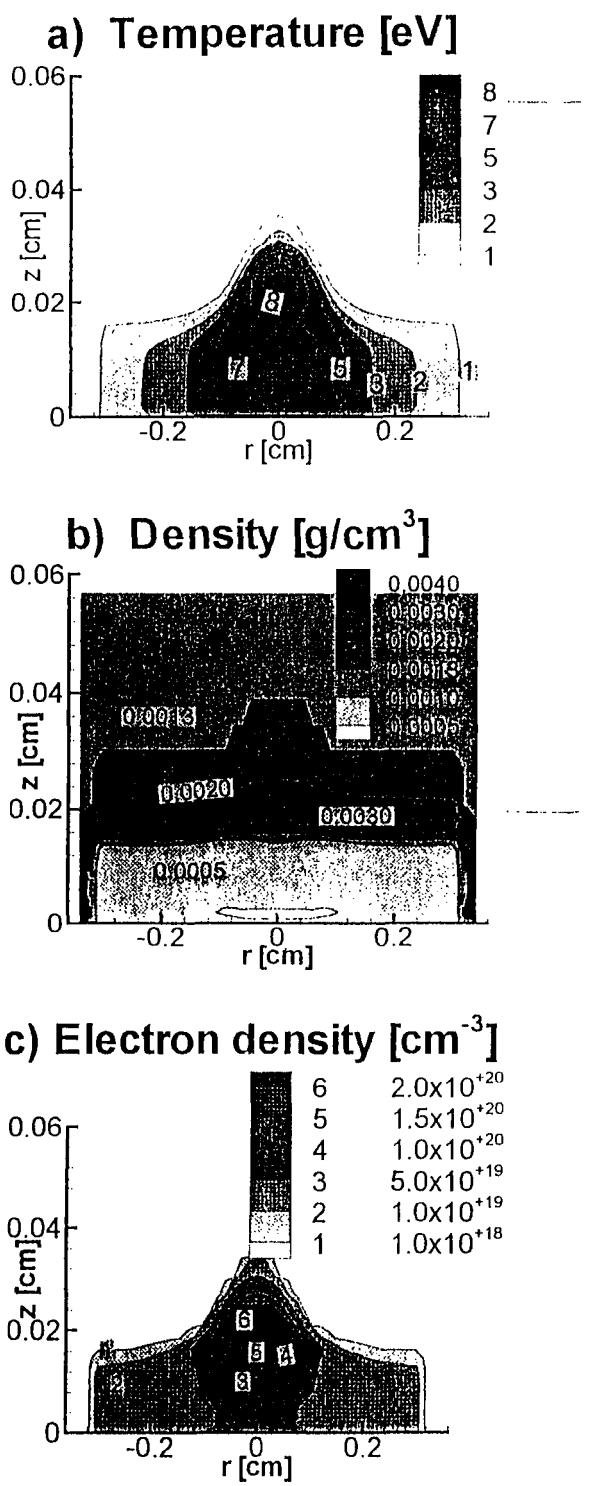

FIG. 8. Contour plots of the computational domain subjected to laser pulse at wavelength $\lambda = 0.353$ μm, at $t = 0$ ns (peak of the pulse): (a) temperature, (b) density, and (c) electron concentration.

decreased by the high pressure in the domain behind the ionization wave, therefore the typical $V_z \approx 6$ km/s is almost twice as low as the velocity of radial expansion [Fig. 7(c)]. At the instant $t \approx 200$ ns the plasma pattern has the form of a half-sphere with radius $r \approx 0.3$ cm.

For the UV effect the expansion of the plasma has qualitative distinctions (Figs. 8 and 9). The plasma absorption rate

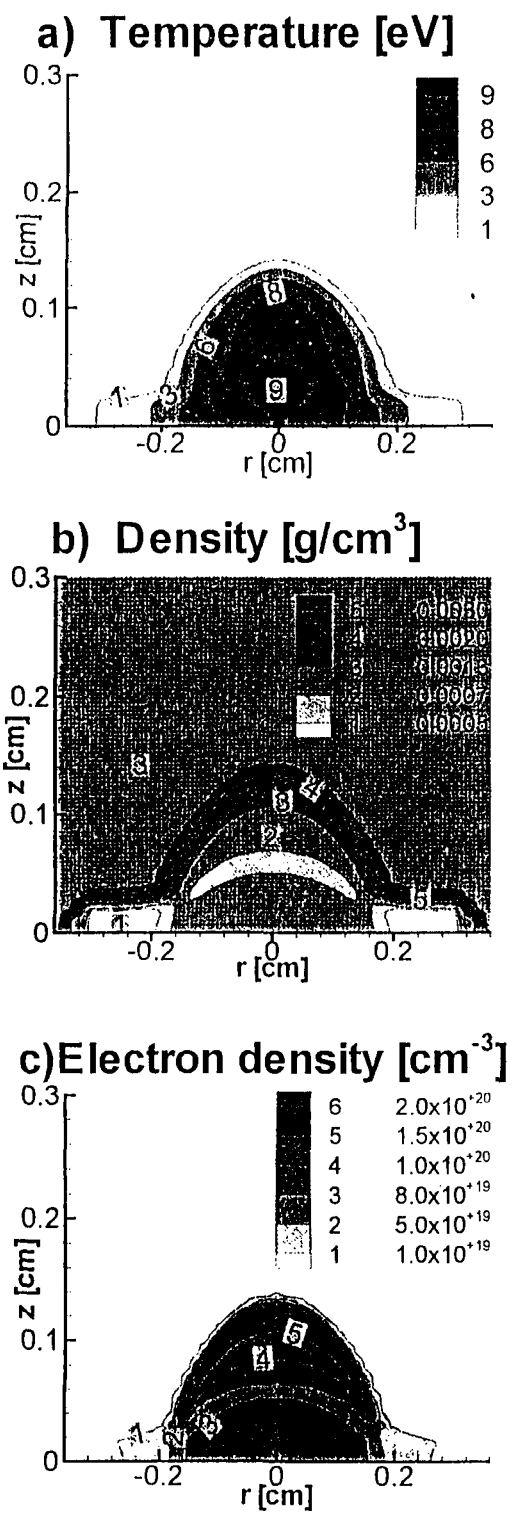

FIG. 9. Contour plots of the computational domain subjected to laser pulse at wavelength $\lambda=0.353$ μm, at $t=34$ ns (completion of the pulse): (a) temperature, (b) density, and (c) electron concentration.

that diminishes with decreasing wavelength is insufficient to support the ionization wave. Screening of the laser radiation proceeds mainly on the shock wave front, leading to the formation of the LSD wave.[18] The ionization front for this regime moves only slightly ahead of the shock wave (Fig. 10).

The contribution of the plasma radiation is also significantly different for the UV effect. Figure 11, similar to Fig. 5 for the IR effect, presents the temperature profiles, determined with and without account of the radiation transfer. The sharp front of the shock wave has the temperature of 8–10 eV and emits a radiation with spectral maximum at the 25–30 eV range. The cold air ahead of the shock wave effectively absorbs in this range, which leads to the formation of a preionization domain, with air being in the partially ionized state (Fig. 11, solid line). For the computation performed with the plasma radiation excluded, the domain ahead of the shock wave remains cold (Fig. 11, dashed line). The plasma radiation also smoothes the shock wave front and decreases temperature in the hot domain.

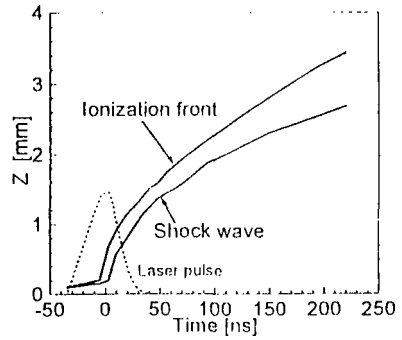

FIG. 10. Coordinates of the shock wave and ionization front, $\lambda=0.353$ μm.

Differences in the plasma expansion regime also manifest themselves on the pressure and velocity distribution (Fig. 12). The shock wave and preionization domains are well seen on the profiles of pressure [Fig. 12(a)]. The normal velocity $V_z \approx 15$ km/s is more than twice that of the IR effect [Fig. 12(b)]. The radial expansion proceeds similar to the IR effect [Fig. 12(c)].

C. Absorption of laser radiation

The laser radiation and plasma interaction is characterized by the absorption coefficient, which depends on three variables $\kappa=\kappa(\nu,T,\rho)$. Two of the variables, the temperature T and the density ρ are dynamic characteristics of the process, while the frequency ν is fixed for the given laser. For the IR range the absorption coefficient has exponential dependence on temperature and linear on density. For the UV

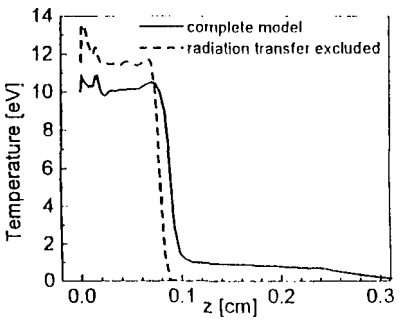

FIG. 11. Temperature distribution $T(z,r=0)$ at $t=17$ ns determined by the complete model (solid line) and by the model with radiation transfer excluded (dashed line), $\lambda=0.353$ μm.

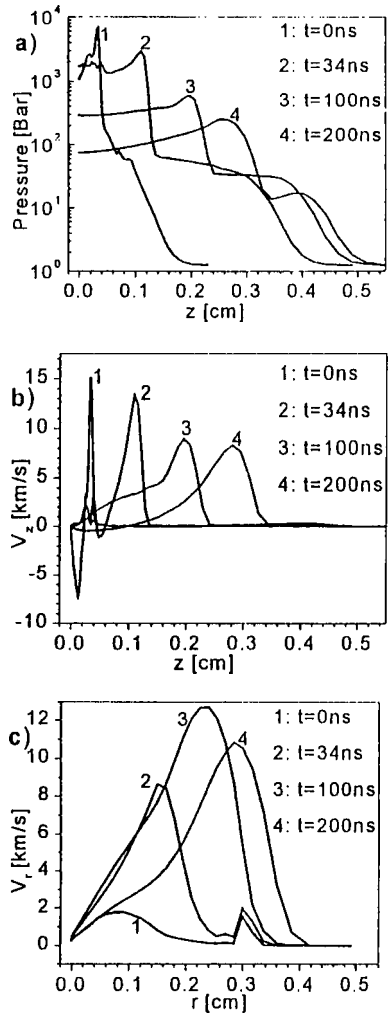

FIG. 12. Distributions of pressure $P(z,r=0)$ (a), velocity components $V_z(z,r=0)$ (b), and $V_r(r,z=55\,\mu\text{m})$ (c) at several instants of time, $\lambda=0.353$ μm.

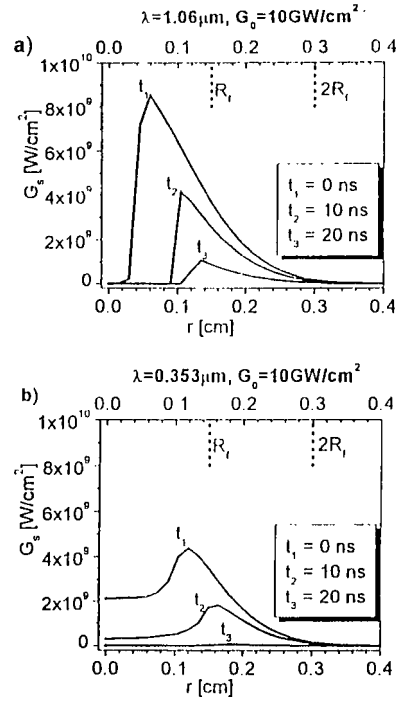

FIG. 13. Spatial plots of laser intensity at the water surface $G_s(r,t)$ for laser effect at $\lambda=1.06$ μm (a) and $\lambda=0.353$ μm (b).

range both dependencies are approximately linear. This distinction leads eventually to different plasma expansion mechanisms.

For the IR effect, the domain of energy release depends primarily on temperature distribution. In the z direction the absorption zone lies near the ionization front and propagates rapidly toward the laser radiation source. Typical values of the absorption coefficient are $(3-4)\times10^2\,\text{cm}^{-1}$, the laser radiation is completely absorbed and does not penetrate deeper to the plasma pattern. The radial distribution of the absorption is illustrated by the $G_s(r,t)$ dependencies of the laser radiation intensity at the water surface [Fig. 13(a)]. The size of the absorption zone is much narrower than the beam radius R, which is explained by the Gaussian intensity distribution $G(r,t)\sim\exp[-(r/R)^2]$ and the high sensitivity of the coefficient κ to the temperature. At the same time the radiation of spatial "wings" of the laser pulse propagates through the plasma unimpeded and reaches the water surface. For example, at the $t=0$, that corresponds to the peak intensity of the laser, the domain $r\leqslant0.04$ cm is completely opaque, $0.04<r<0.06$ cm is partially opaque and $r\geqslant0.06$ cm is transparent [Fig. 13(a)]. Later on the opaque domain broadens and a more significant part of the incident radiation is absorbed. The sharp boundary of absorption domain along the r axis is also well seen on the temperature plots [Figs. 2(a) and 3(a)]. The integration of $G_s(r,t)$ on time and space yields that $\approx85\%$ of the laser energy reaches the surface of the condensed medium.

The reradiation of the plasma can play an important role for the IR effect. Presented in Fig. 14(a) are $W_s(r,t)$ profiles of the plasma radiation flux at the water surface. The maximum value of the $W_s(r,t)$ is reached at $r=0$, $t=17$ ns and is equal to $\approx3\times10^8\,\text{W/cm}^2$. Though the plasma radiation flux is significantly lower than the laser flux, its effect can be significant, because it penetrates the domain where the laser radiation is absent. The plasma reradiates $\approx10\%$ of the absorbed energy of the laser pulse, and thus the total fraction of the energy transmitted to the condensed medium is $\approx87\%$.

For the UV effect the absorption of plasma is controlled primarily by density distribution and the maximum of energy release is at the shock wave domain. The typical values of the absorption coefficient are much lower as compared to the IR effect $\kappa\approx(20-50)\,\text{cm}^{-1}$. It means that the size of energy release zone along the z axis $\sim\kappa^{-1}$ is comparable to the size of the plasma pattern. The absorption of the laser energy in the radial direction proceeds in the domain comparable to the beam radius $r\leqslant R$ [Fig. 13(b)], however, the plasma does not shield the laser radiation completely. The transmitted flux has maximum $G_s\approx4\times10^9\,\text{W/cm}^2$ at $t=0$ and $r\approx R_f$. The flux of the plasma radiation $W_s(r,t)$ is as high as $\approx8\times10^8\,\text{W/cm}^2$ [Fig. 14(b)], the reradiation effect is stronger and amounts to 25% of the absorbed energy. Totally, $\approx75\%$ of the laser pulse energy is transmitted to the condensed medium for the UV effect, which makes it smaller than for the IR effect.

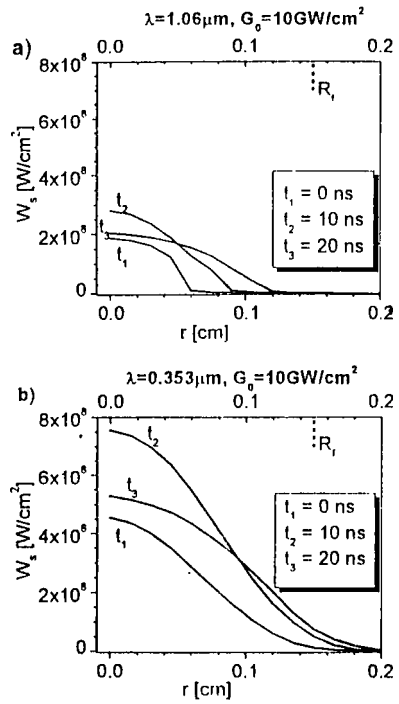

FIG. 14. Spatial plots of plasma radiation flux at the water surface $W_s(r,t)$ for laser effect at $\lambda=1.06$ μm (a) and $\lambda=0.353$ μm (b).

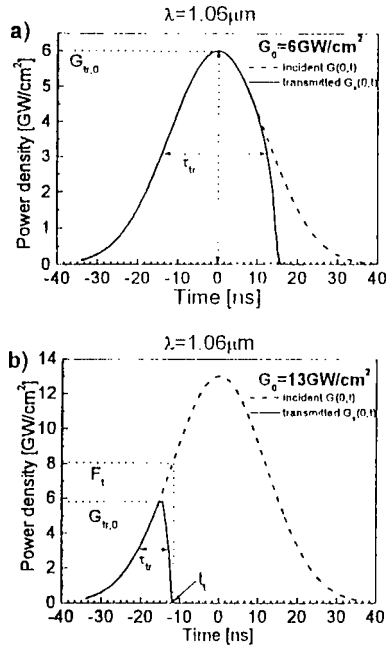

FIG. 15. Plots of incident $G(0,t)$ and transmitted $G_s(0,t)$ laser radiation for laser effect at wavelength $\lambda=1.06$ μm with intensity of $G_0=6$ GW/cm^2 (a), and $G_0=13$ GW/cm^2 (b).

The maximum concentration of electrons reached in the plasma also presents important characteristics for the plasma-laser radiation interaction. If the critical density of electrons $N_{e,\mathrm{crit}}=m\omega^2/4\pi e^2$, ω being the laser frequency is reached, the plasma becomes completely opaque and reflects the incident laser radiation. The $N_{e,\mathrm{crit}}$ values are 9.82×10^{20}, 4.18×10^{21}, and 8.84×10^{21} cm^{-3} for the considered wavelengths of radiation 1.06, 0.514, and 0.353 μm appropriately, while according to the predictions of the model the plasma concentration does not exceed 5×10^{20} cm^{-3} for the intensity range 4–17 GW/cm^2. It means that the critical density of electrons is not reached and the main mechanism that shields the laser radiation is the plasma absorption.

D. Transmitted pulse parameters

Due to the plasma absorption, the transmitted laser pulse has smaller intensity $G_s(r,t)$ and duration τ_{tr} as compared to $G(r,t)$ and τ of the incident one. In this paragraph variations of transmitted pulse parameters are considered depending on the peak intensity G_0. Presented in Figs. 15 and 16 are time dependencies of the incident $G(0,t)$ and transmitted pulses $G_s(0,t)$ in the center of the focal spot $r=0$ predicted for the IR and UV irradiation with intensity of $G_0=6$ GW/cm^2 and $G_0=13$ GW/cm^2.

For the IR effect at $G_0=6$ GW/cm^2 [Fig. 15(a)] plasma initiates only at the end of the incident pulse $t\approx12$ ns and the screening effect is weak. As a consequence, the parameters of the transmitted pulse: peak intensity $G_{\mathrm{tr},0}$ and width τ_{tr}, are approximately the same as the ones of the incident pulse. For the effect of $G_0=13$ GW/cm^2 the screening starts already at the leading edge of the pulse $t\approx-17$ ns [Fig. 15(b)], therefore the transmitted pulse appears to be approximately two times weaker, $G_{\mathrm{tr},0}\approx6$ GW/cm^2, and three times shorter, $\tau_{\mathrm{tr}}\approx10$ ns. So as the output intensity of the laser equipment is increased, the intensity of the effective (transmitted) pulse remains constant and the duration even diminishes.

For the UV effect of $G_0=6$ GW/cm^2 and $G_0=13$ GW/cm^2 screening begins at the leading edge in both cases (Fig. 16). However, the optical thickness of plasma increases much more slowly and as a result, the two transmitted pulses have approximately the same intensity and du-

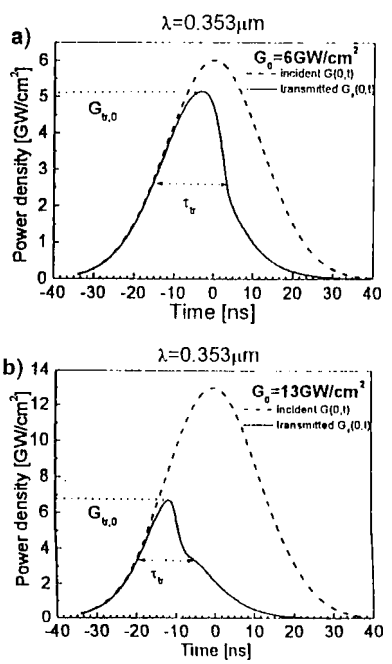

FIG. 16. Plots of incident $G(0,t)$ and transmitted $G_s(0,t)$ laser radiation for laser effect at wavelength $\lambda=0.353$ μm with intensity of $G_0=6$ GW/cm^2 (a), and $G_0=13$ GW/cm^2 (b).

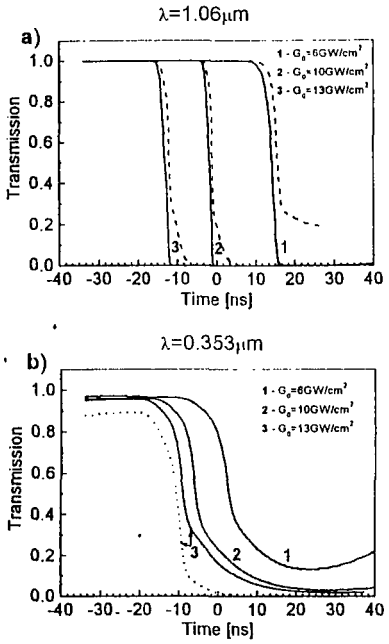

FIG. 17. Transmission coefficient of plasma for laser effect at wavelength $\lambda=1.06$ μm (a) and $\lambda=0.353$ μm (b) with intensity of $G_0=6$ GW/cm^2 (1), $G_0=10$ GW/cm^2 (2), and $G_0=13$ GW/cm^2 (3). Dashed lines indicate the transmission coefficient of the probe laser radiation $\lambda=0.514$ μm.

ration: $G_{tr,0}\approx 6$ GW/cm^2, $\tau_{tr}\approx 15$ ns at the $G_0=6$ GW/cm^2, and $G_{tr,0}\approx 7$ GW/cm^2, $\tau_{tr}\approx 15$ ns at the $G_0=13$ GW/cm^2

The transmission coefficients of plasma, defined as $Tr(t)=G_s(0,t)/G(0,t)$ are presented in Fig. 17. This quantity, in particular, allows to determine the time over which the plasma becomes opaque (optically thick). This time is 3–5 ns for the IR effect [Fig. 17(a)] and 20–30 ns for the UV effect [Fig. 17(b)]. At the UV effect of $G_0=6$ GW/cm^2 [Fig. 17(b), curve 1], the plasma does not screen radiation completely and the transmission coefficient starts to increase at the end of the pulse because of gas-dynamic expansion.

Also, indicated in Fig. 17(a) are the transmission plots determined for the radiation of the probe laser at $\lambda=0.514$ μm. The radiation is screened less effectively due to a shorter wavelength. For example, if the time t_{tr} is estimated when the transmission coefficient becomes equal to 0.5, the introduced error is 2–3 ns. For the UV effect [Fig. 17(b)], the probe radiation is screened more effectively than the main laser radiation.

E. Comparison with experiment

A series of computations for the IR effect is presented in Figs. 18 and 19. The intensity G_0 is varied in the interval 6–17 GW/cm^2, and the transmitted pulse parameters $G_{tr,0}$ and τ_{tr} are determined for every computation. The peak intensity of the transmitted pulse first rises up (Fig. 18, solid line) then has maximum and reaches some level of saturation approximately equal to 6 GW/cm^2. Presented in the figure is also the plot of an experimental estimation F_{tr} (dotted line).[8] The numerical predictions coincide well with the experimental values in the $G_0<12$ GW/cm^2, but at a higher intensity the experimental curve approaches the level of saturation

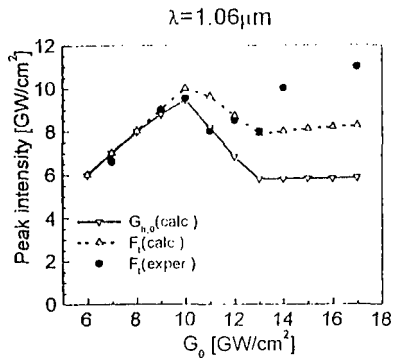

FIG. 18. Dependence of peak intensity of the transmitted pulse on the incident pulse intensity, $\lambda=1.06$ μm: numerical prediction $G_{tr,0}(G_0)$, experimental estimation $F_t(G_0)$ (see Ref. 8), and numerical prediction for $F_t(G_0)$.

≈ 10 GW/cm^2, with an experiment accuracy of ± 2 GW/cm^2. One of the reasons for the two plot deviation is due to the different transmission of plasma at the 1.06 and 0.514 μm (see Sec. III D). The other reason originates from the technique of experimental estimation itself, which includes two steps: (i) the instant of time t_{tr} is determined when the transmission Tr is equal to 0.5, $Tr(t_{tr})=0.5$; and (ii) the value of the laser intensity at the moment t_{tr} is taken as the estimation of the transmitted pulse intensity $G(t_{tr})\equiv F_{tr}$. The described technique is illustrated in Fig. 15(b), and it is obvious that the respective deviation is significant. The numerically determined $F_{tr}(G_0)$ curve is also presented in Fig. 18, dashed line. The $G_{tr,0}$ and F_{tr} deviation can be as high as 2–3 GW/cm^2.

The duration of the transmitted pulse $\tau_{tr}(G_0)$, both determined numerically and taken from Ref. 8, is shown in Fig. 19, solid and dotted lines, respectively. The pulse width diminishes from the maximum of 25–30 ns to the constant level ≈ 8 ns, while the experimental curve saturates at 10–15 ns. The reason for this deviation besides the already mentioned factor of wavelength, is the difference of precise Gaussian dependence used in computations and the experimental pulse shape. The difference is negligible for the consideration of the entire pulse, but becomes more significant if the analysis deals with the wings of the pulse.

Also the dependencies of $G_{tr,0}(G_0)$ and $\tau_{tr}(G_0)$ are determined for the UV effect at the intensity G_0 of 4–15

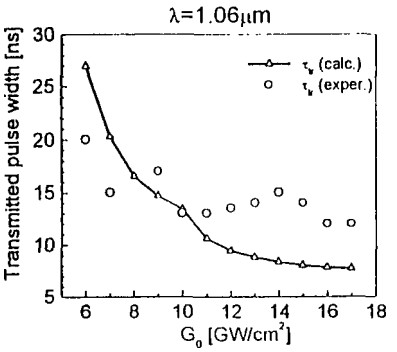

FIG. 19. Dependence of the transmitted pulse duration on the incident pulse intensity $\tau_{tr}(G_0)$, $\lambda=1.06$ μm: predicted numerically (solid line) and determined experimentally (dotted line) (see Ref. 8).

GW/cm^2. The respective results are similar to the ones for the IR effect. As G_0 increases, the peak intensity of the transmitted pulse $G_{tr,0}$ saturates at 6 GW/cm^2, and the width of the transmitted pulse τ_{tr} approaches the steady-state value of $\approx$15 ns, which is twice as great as for the IR effect.

IV. CONCLUSION

The results of the modeling of an air plasma induced by IR λ=1.06 μm or UV λ=0.355 μm laser radiation of the intensity range 4–17 GW/cm^2 are presented. The results indicate strong nonlinear coupling between thermal, radiation, and gas-dynamic processes in the plasma. The interaction of the processes, ultimately, determines plasma transmission, which is the basic parameter of optimization on the irradiation regime. The analysis of the results allows one to conclude:

(1) The dynamics of plasma expansion for the IR and UV effect have significant differences. For the IR effect the main expansion mechanism is the fast propagation of the ionization wave toward the laser source. It is just the ionization wave that absorbs the major part of the laser radiation in this case. For the UV effect the plasma expands in the form of the LSD wave, and is mainly influenced by relatively slow gas-dynamic processes.

(2) The typical plasma temperature and maximum electron concentration predicted are $\approx$10 eV and $\approx 5 \times 10^{20}\,\mathrm{cm}^{-3}$, the critical electron concentration for the considered radiation wavelengths are not reached.

(3) The plasma radiation contributes significantly to the redistribution of energy inside the plasma domain and, for the UV effect, forms the domain of pre-ionization ahead of the shock wave.

(4) For the UV effect the plasma absorption manifests itself at lower intensity, but the time needed for plasma to become completely opaque is 20–30 ns, while for the IR effect the process takes only 3–5 ns.

(5) As the intensity of the laser effect is increased, the peak intensity of the transmitted pulses reaches a level of saturation, which is approximately equal for the IR and UV effect, but for the latter the transmitted pulse is twice as long.

The proposed model presents an effective tool for the analysis of the air plasma in the wide range of laser effect parameters used in laser shock processing.

ACKNOWLEDGMENTS

The work was partially supported by the European Commission under the Copernicus CP96-0080 Project (VITEWE). The authors acknowledge the recommendations and research results provided by R. Fabbro and L. Berthe in the course of this study.

[1] A. H. Clauer, B. P. Fairand, and J. Holbrook, in *Shock Waves and High Strain Phenomena in Metals—Concepts and Applications*, edited by L. Murr (Plenum, New York, 1981), p. 675.
[2] P. Peyre, R. Fabbro, L. Berthe, and C. Dubouchet, J. Laser Appl. **8**, 135 (1996).
[3] B. P. Fairand and B. A. Wilcox, J. Appl. Phys. **43**, 3893 (1972).
[4] H. K. Park, D. Kim, and C. Grigoropoulos, J. Appl. Phys. **80**, 4072 (1996).
[5] L. Berthe, R. Fabbro, P. Peyre, L. Toillier, and E. Bartnicki, J. Appl. Phys. **82**, 2826 (1997).
[6] L. Berthe, R. Fabbro, P. Peyre, and E. Bartnicki, J. Appl. Phys. **85**, 7552 (1999).
[7] R. Fabbro, P. Peyre, L. Berthe, A. Sollier, and E. Bartnicki, Proc. SPIE **3888**, 155 (2000).
[8] L. Berthe, R. Fabbro, P. Peyre, and E. Bartnicki, Eur. Phys. J.: Appl. Phys. **3**, 215 (1998).
[9] S. V. Gribin, I. I. Komissarova, G. V. Ostrovskaja, B. I. Spesivcev, V. N. Phylippov, and E. N. Shvedova, J. Tech. Phys. **70**, 64 (2000).
[10] D. C. Emmony, I. Geerken, and H. Klein-Baltink, J. Acoust. Soc. Am. **73**, 220 (1983).
[11] S. V. Egerev, L. M. Lamshev, and K. A. Naugolnich, Akusticheskii J. **31**, 277 (1985).
[12] M. Aden, E. Beyer, R. Herziger, and H. Kunze, J. Phys. D **25**, 57 (1992).
[13] A. Vertes, R. W. Dreyfus, and D. E. Platt, IBM J. Res. Dev. **38**, 3 (1994).
[14] C. Phipps and R. Dreyfus, in *Laser Microprobe Mass Analysis*, edited by A. Vertes, R. Gijbels, and F. Adams (Wiley, New York, 1993).
[15] H. Schittenhelm, G. Callies, P. Berger, and H. Hugel, J. Phys. D **29**, 1564 (1996).
[16] H. Schittenhelm, G. Callies, P. Berger, and H. Hugel, J. Phys. D **31**, 418 (1998).
[17] M. F. Modest, *Radiative Heat Transfer* (McGraw-Hill, New York, 1993).
[18] Yu. P. Raizer, *Physics of Gas Discharge* (Nauka, Moscow, 1987).
[19] B. N. Chetverushkin, *Dynamics of Radiative Gas* (Nauka, Moscow, 1992).
[20] Ya. B. Zeldovich and Yu. P. Raizer, *Physics of Shock Waves and High Temperature Hydrodynamics Phenomena I* (Academic, New York, 1967).
[21] V. I. Mazhukin, A. A. Uglov, and B. N. Chetverushkin, Dokl. Akad. Nauk SSSR **256**, 1100 (1981).
[22] V. I. Mazhukin, I. Smurov, and G. Flamant, J. Comp. Phys. **112**, 78 (1994).
[23] V. I. Mazhukin, S. G. Gorbachenko, I. Smurov, G. Flamant, and A. Gleizes, Proceedings of the 6th European Conference on Laser Treatment of Materials ECLAT-96, Stuttgart, 1996.
[24] V. I. Mazhukin and G. A. Pestrjakova, Vichisel. Matem. **25**, 1697 (1985).
[25] V. I. Mazhukin and A. A. Samarskii, Surv. Math. Ind. **4**, 85 (1994).
[26] M. A. Elyashevich, L. Ya. Minko, G. S. Romanov, Yu. A. Stankevich, Yu. A. Chivel, and A. N. Chumakov, Izv. Akad. Nauk. Ser. Fiz. **49**, 1132 (1985).
[27] J. R. Ho, C. P. Grogoropulus, and J. A. C. Humphrey, J. Appl. Phys. **79**, 7205 (1996).
[28] J. P. Jackson and P. E. Welsen, AIAA J. **12**, 1498 (1974).
[29] V. A. Kamenshikov, J. A. Plastinin, V. M. Nikolaev, and L. A. Novickij, *Radiative Properties of Gases at High Temperatures* (Mashinostrojenije, Moscow, 1971).
[30] N. N. Kalitkin, L. V. Kuzmina, and V. S. Rogov, Preprint No. 21 of IPM AN SSSR, 1972.
[31] *Reactions Under Plasma Conditions I*, edited by M. Venugopalan (Wiley-Interscience, New York, 1970).
[32] R. Fabbro and L. Berthe (private communication).
[33] V. I. Mazhukin, V. V. Nossov, I. Smurov, R. Fabbro, L. Berthe, P. Peyre, and A. Sollier, EMRS-1999 Book of Abstracts, A-V/59.